



Rapid crystallization of precious-metal-mineralized layers in mafic magmatic systems

Luke N. Hepworth^{1,2}, J. Stephen Daly^{3,4}, Ralf Gertisser¹, Chris G. Johnson⁵, C. Henry Emeleus^{6,7} and Brian O'Driscoll¹✉

The solidified remnants of mafic magmatic systems host the greatest concentrations of platinum-group metals in the Earth's crust. Our understanding of precious-metal mineralization in these intrusive bodies is underpinned by a traditional view of magma chamber processes and crystal mush solidification. However, considerable uncertainty remains regarding the physical and temporal controls on concentrating these critical metals, despite their importance to modern society. We present high-precision ⁸⁷Sr/⁸⁶Sr analyses of plagioclase and clinopyroxene from within centimetre-thick precious-metal-enriched layers in the Palaeogene open-system Rum layered intrusion (northwest Scotland). Isotopic heterogeneity is present between plagioclase crystals, between clinopyroxene and plagioclase and within plagioclase crystals throughout the studied section. On the basis of these observations, we demonstrate that platinum-group element mineralization formed by repeated small-volume reactive melt percolation events. The preservation of strontium isotope heterogeneities at 10–100 μm length scales implies cooling of the melts that formed the precious-metal-rich layers occurred at rates greater than 1°C per year, and cooling to diffusive closure within tens to hundreds of years. Our data highlight the importance of cyclic dissolution–recrystallization events within the crystal mush and raise the prospect that precious-metal-bearing mafic intrusions may form by repeated self-intrusion during cooling and solidification.

A small number of mafic(–ultramafic) intrusive systems, so-called layered intrusions, are responsible for supplying most of society's platinum (Pt), palladium (Pd) and rhodium (Rh)^{1–3}. A wealth of field, petrological and geochemical information exists for precious-metal deposits in economically significant layered intrusions^{2,4,5}. However, uncertainty persists regarding the mechanisms that concentrate precious metals in centimetre- to metre-thick layers in these intrusions^{1,6}. Some models call for ore-forming processes that acted at or close to the putative magma chamber floor^{6–8}, whereas others invoke relatively low-temperature fluid-rock interactions operating on partly to completely solidified assemblages^{6,9,10}. This disparity means that there is uncertainty around the temperature and rheology of solidifying crystal mushes during platinum-group element (PGE) concentration.

Improving our understanding of the behaviour of solidifying crystal mushes is therefore central to advancing our knowledge of precious-metal enrichment in crustal magmatic systems. Studies of layered intrusions have provided a broad physicochemical framework for understanding how crystal mushes form as cumulates and during postcumulus modification^{11,12}. Melt percolation, reactive flow, melt segregation and mush compaction might all play important roles during solidification¹³. However, critical gaps remain in our understanding of the length- and timescales over which these processes occur. This is especially important in open magmatic systems where rejuvenation of crystal mushes occurs following input of relatively hot primitive magma, increasing mush permeability and leading to reactive through-flow of melt, resulting in a more protracted solidification history^{13–15}. Here, we investigate PGE-rich cumulates of the classic Rum layered intrusion (northwest Scotland, Supplementary Fig. 1) to better constrain the drivers

and timescales of crystallization of precious-metal-mineralized layers in mafic magmatic systems. Our new microsampled plagioclase and clinopyroxene strontium isotope (⁸⁷Sr/⁸⁶Sr) data unambiguously show isotopic heterogeneities at length scales of 10–100 μm that can be linked to reactive percolation events within the Rum crystal mush. From these observations, we calculate that individual PGE-rich layers on Rum were emplaced and closed to diffusive equilibration within hundreds of years, a conclusion that lends strong support to the idea that mafic intrusive systems may also exist in 'cold storage' and be rejuvenated by new magma input, similar to their silicic counterparts^{13–16}.

Magma chamber processes and PGEs in the Rum intrusion

The Rum layered intrusion (British Palaeogene Igneous Province) has been a cornerstone for understanding open-system magmatic and subvolcanic processes for decades^{17–19}. Rum is a particularly valuable locality to investigate unresolved questions relating to the timing of PGE mineralization in layered intrusions. It is well characterized and superbly exposed and, although not exploited for PGEs, it has mineralized layers that are enriched to ppm levels in Pt and Pd²⁰. The intrusion was emplaced ~60 million years ago²¹ (during opening of the Northeast Atlantic) and is much younger than several layered intrusions that host economically significant PGE deposits (for example, the Archaean Stillwater Complex and the Proterozoic Bushveld Complex)^{17,22}, meaning that the age correction required for strontium isotope data in minerals such as plagioclase and clinopyroxene is negligible²³. The eastern portion of the Rum intrusion (Eastern Layered Intrusion) is constructed of 16 macro-rhythmic units, each ~10–100-m thick and composed of a peridotitic base and a gabbroic top. This arrangement has been interpreted to reflect

¹School of Geography, Geology and the Environment, Keele University, Keele, UK. ²Department of Earth and Environmental Sciences, University of Manchester, Manchester, UK. ³UCD School of Earth Sciences, University College Dublin, Dublin, Ireland. ⁴Irish Centre for Research in Applied Geosciences, Dublin, Ireland. ⁵Department of Mathematics, University of Manchester, Manchester, UK. ⁶Department of Earth Sciences, Durham University, Durham, UK. ⁷Deceased: C. Henry Emeleus. ✉e-mail: brian.odriscoll@manchester.ac.uk

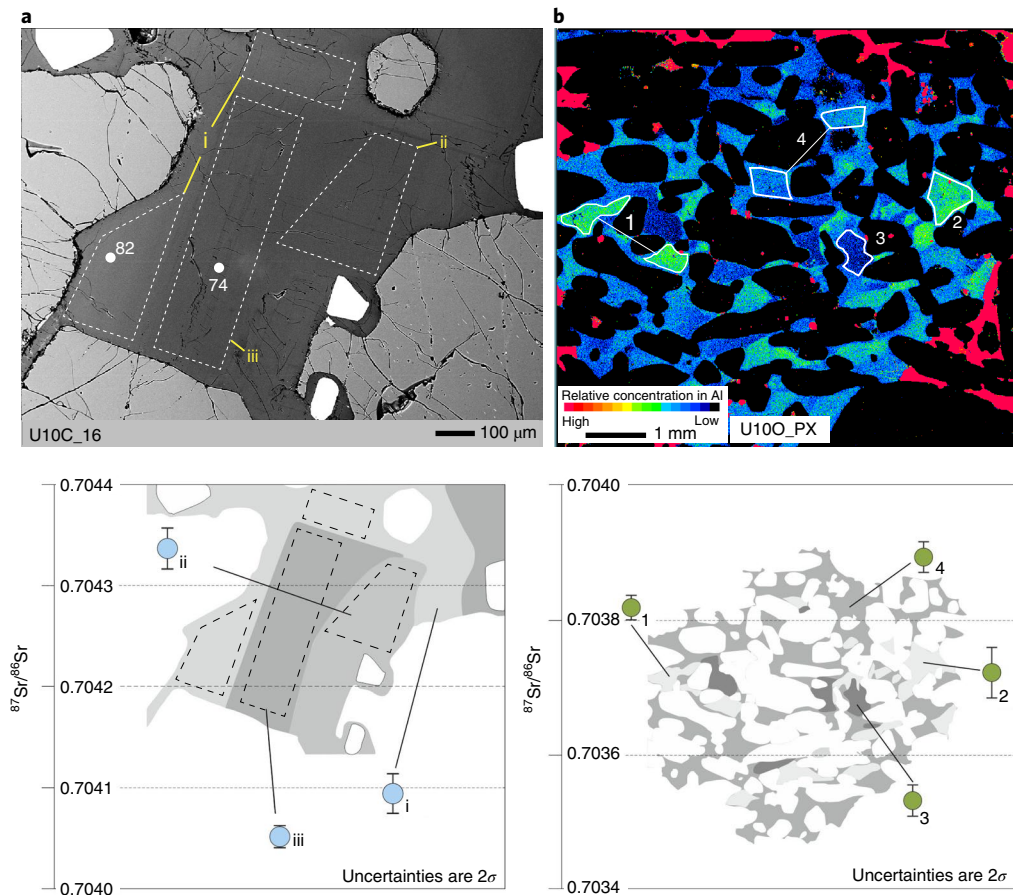


Fig. 1 | Examples of intracrystalline $^{87}\text{Sr}/^{86}\text{Sr}$ variation in Unit 10 plagioclase and clinopyroxene. **a**, Back-scattered electron micrograph and corresponding interpretive sketch with $^{87}\text{Sr}/^{86}\text{Sr}$ data (with 2σ uncertainties) for U10C_16. The white spots/numbers are EMPA analysis points with corresponding anorthite content. The dashed white outlines delineate the microdrilled pits. For i, material was drilled from two pits in the same (interpreted) plagioclase zone. **b**, Element map (aluminium (Al)) of clinopyroxene oikocryst (U10O_PX). The microdrilled portions of the oikocryst are outlined in white. For 1 and 4, this comprises two drilled pits each. The $^{87}\text{Sr}/^{86}\text{Sr}$ data are shown below in the interpretive sketch.

fractionation of olivine and then plagioclase from successive batches of basaltic or picritic magma¹⁸. The ~80-m-thick Unit 10 package has been held up as an important example of fractional crystallization of magma for >60 yr (ref. ¹⁸) on the basis of broad trends in mineral chemistry (for example, olivine forsterite contents) and bulk rock $^{87}\text{Sr}/^{86}\text{Sr}$ compositions (Supplementary Fig. 1)²⁴. It is subdivided into four sections as follows: the lower peridotite (~40 m), upper peridotite (~20 m), troctolite (~5 m) and olivine gabbro (~15 m)^{18,24}.

More recently, it has been suggested that at least 20–30% of the Unit 10 peridotite formed by late-stage addition of aphyric (picritic) and olivine-phyric magmas in small-volume intrusions²⁵. In particular, the lower peridotite contains numerous 10- to 50-cm-thick texturally distinct peridotite layers that exhibit intrusive relationships with the peridotite above and below. Hundreds of millimetric chromium- (Cr-) spinel seams have been documented throughout the lower peridotite²⁵ (contextual petrological detail for these is provided in Extended Data Figs. 1–3). These Cr-spinel seams are mainly several millimetres to centimetres thick and contain base-metal sulfides (for example, pentlandite, pyrrhotite and chalcopyrite) and platinum-group minerals (for example, sulfides, arsenides and tellurides). The Cr-spinel seams are stratiform but not stratabound; they are mainly confined to discrete layer boundaries (defined by olivine grain-size changes) but may locally cut up or down into host peridotites (see ref. ²⁵ for further detail). Some Cr-spinel seams bifurcate. A key observation is that intercumulus plagioclase within 1–2 cm on either side of Cr-spinel seams is ubiquitously

compositionally zoned (for example, Extended Data Fig. 2). Zoning can be normal, reverse or oscillatory in nature, but more-complex compositional zoning is also typical. Importantly, zoning of intercumulus plagioclase in the Unit 10 peridotites away from Cr-spinel seams is much less common or absent²⁵. In the upper peridotite, Cr-spinel seams are absent²⁵. The upper peridotite predates the lower peridotite and its ubiquitous ~1-cm-sized diopside oikocrysts may reflect a metasomatic overprint as a result of upward-migrating melts^{25–27}. At the top of the upper peridotite, an ~20-cm thick pegmatite body occurs at the boundary with the overlying troctolite.

Target samples and intracrystalline strontium isotope variation

Intercumulus crystals form from the interstitial melt in the crystal mush, so they may record evidence of melt–rock interaction after the primary accumulation of the cumulus crystal framework. To investigate the intercumulus minerals close to the Cr-spinel seams, three such seams (U10A, U10B and U10C, documented further in ref. ²⁵) were sampled from an ~3 m interval in the middle of the lower peridotite (Supplementary Fig. 1). One of these seams (U10B) occurs along the contact with an intrusive peridotite, but the other two lack this association. Major element chemistry and compositional maps were collected on these samples by electron microprobe (see Methods and Extended Data Figs. 4 and 5, and Supplementary Tables 1–3 in Supplementary Data 1). Zoned intercumulus plagioclase crystals were then selected from the three seams for strontium isotopic

Table 1 | Strontium isotope data for plagioclase and clinopyroxene from the Rum layered intrusion

Plagioclase	⁸⁷ Sr/ ⁸⁶ Sr	2σ (error)
Unit 10		
U10_PEG_ii	0.704289	0.000015
U10_PEG_i	0.704337	0.000012
U10O_1_ii	0.704026	0.000017
U10O_1_i	0.704259	0.000020
U10C_16_iii	0.704052	0.000011
U10C_16_ii	0.704337	0.000020
U10C_16_i	0.704095	0.000020
U10C_13_i	0.704306	0.000045
U10C_4_ii	0.704095	0.000009
U10C_4_i	0.704134	0.000007
U10B_1_ii	0.704591	0.000008
U10B_1_i	0.704517	0.000009
U10A_12_iii	0.704099	0.000016
U10A_12_ii	0.704098	0.000011
U10A_12_i	0.704141	0.000014
Unit 8		
U8_20_ii	0.703956	0.000009
U8_20_i	0.703943	0.000014
Western Layered Intrusion		
HAR-v	0.703202	0.000010
HAR-iv	0.703172	0.000027
HAR-iii	0.703148	0.000014
HAR-ii	0.703178	0.000011
HAR-i	0.703328	0.000016
Clinopyroxene		
	⁸⁷ Sr/ ⁸⁶ Sr	2σ (error)
Unit 10		
U10PEG-PX_i	0.704517	0.000017
U10PEG-PX_ii	0.704321	0.000034
U10PEG-PX_iii	0.704180	0.000021
U10O-PX_1	0.703819	0.000018
U10O-PX_2	0.703723	0.000037
U10O-PX_3	0.703533	0.000023
U10O-PX_4	0.703894	0.000023
U10B-PX_ii	0.704296	0.000032
U10B-PX_i	0.704243	0.000031

See text for discussion and description of abbreviations used. See Supplementary Table 4 in Supplementary Data 1 for further detail.

analysis (for example, Fig. 1a). A clinopyroxene from sample U10B was also analysed. One zoned clinopyroxene oikocryst and a zoned plagioclase were analysed from the upper peridotite (U10O; Fig. 1b), as well as both plagioclase and clinopyroxene from the troctolite body occurring between the upper peridotite and the troctolite (U10PEG). We also report strontium isotope data for intercumulus plagioclase in a Cr-spinel seam from Unit 8 (U8) of the Eastern Layered Intrusion and from a Western Layered Intrusion peridotite (HAR-1). Sampling of individual intracrystal zones in plagioclase and clinopyroxene was carried out using a New Wave Micromill, and unspiked strontium isotopic analyses were performed by thermal ionization mass spectrometry (see Methods).

The new ⁸⁷Sr/⁸⁶Sr data are reported in Table 1 and Figs. 1 and 2 (see also Supplementary Tables 4 and 5 in Supplementary Data 1). Anhedral intercumulus plagioclase crystals exhibit highly irregular zoning, including dissolution surfaces. Overall, they range in composition between labradorite and bytownite (An_{61–86}). Their K₂O and TiO₂ contents correlate negatively with anorthite content, and plagioclase is ubiquitously more anorthitic where it contains Cr-spinel crystals. Plagioclase Sr concentrations mostly range between 250 and 500 ppm, and barium (Ba) and rubidium (Rb) concentrations are consistently <1 ppm. Clinopyroxene is close to endmember diopside in composition. Electron microprobe element maps reveal that the studied clinopyroxene oikocryst in U10O contains complex, patchy zoning, with a positive correlation observed between Cr₂O₃ and Al₂O₃.

Most of the analysed crystals reveal inter- and intracrystalline isotopic heterogeneity. The maximum range (with 2σ uncertainties) of ⁸⁷Sr/⁸⁶Sr is 0.704026 ± 17 to 0.704591 ± 8 in the Unit 10 plagioclase and 0.703533 ± 23 to 0.704517 ± 17 in clinopyroxene. Within a single, oscillatory-zoned plagioclase, three discrete zones yielded ⁸⁷Sr/⁸⁶Sr values of 0.704337 ± 20, 0.704095 ± 20 and 0.704052 ± 11 (Fig. 1a). The complex patchily zoned clinopyroxene oikocryst yielded a ⁸⁷Sr/⁸⁶Sr range of 0.703533 ± 23 to 0.703894 ± 23 (Fig. 1b). Isotopic disequilibrium also occurs within plagioclase, within clinopyroxene and between the phases in the pegmatite (Fig. 2). The strontium isotopic variations broadly correspond to major element variation in both plagioclase and clinopyroxene. In the case of plagioclase crystals in the Cr-spinel seams, more-anorthitic plagioclase, as illustrated by its brighter back-scattered electron intensity, tends to be characterized by more radiogenic ⁸⁷Sr/⁸⁶Sr values (Fig. 1a). In the clinopyroxene, low Al₂O₃ (and Cr₂O₃) domains within the oikocryst are characterized by less radiogenic ⁸⁷Sr/⁸⁶Sr.

Reactive melt percolation in the Unit 10 crystal mush

The Cr-spinel seams represent sites of highly localized reactive melt flow in the lower peridotite crystal mush (Fig. 3). This conclusion is based on the intercumulus nature of the zoned plagioclase, the locally transgressive nature of the seams and the 10–100 μm strontium isotope heterogeneities. Simultaneous dissolution of olivine and plagioclase during melting will lead to precipitation of spinel (plus anorthite or forsterite) at a temperature of ~1,320 °C (ref. 28). The coincidence of Cr-spinel with anorthitic plagioclase in the interstitial areas of the seams, and absence of Cr-spinel from areas where the plagioclase is more sodic, suggests that Cr-spinel crystallized in situ during a peritectic reaction within the crystal mush. Picrite melts such as those considered to be the parental melts of the Rum intrusion are considered to have liquidus temperatures on the order of ~1,350 °C (refs. 22,29), so there was probably sufficient heat to drive dissolution. Most of the Unit 10 Cr-spinel seams are up to 1-cm thick, and have a framework of ~30–40 vol.% cumulus olivine, so reactive through-flow of melt was facilitated by the implied high porosity. The Unit 10 Cr-spinel seams are therefore best interpreted as high-flux (high melt/rock ratio) percolation zones, and the resulting seam dimensions represent minimum thicknesses and lengths of these zones. Along-strike variation of the percolation zones, including thickness variations, discontinuities and narrowing to tears within the crystal mush, are all consistent with the field relations (details in Fig. 3).

In a given crystal, the most-anorthitic plagioclase zones tend to have more radiogenic Sr, supporting the suggestion that assimilation of feldspathic cumulate with radiogenic ⁸⁷Sr/⁸⁶Sr drove Cr-spinel crystallization²². This is consistent with the field relations since the Unit 10 troctolite predates the lower peridotite and has ⁸⁷Sr/⁸⁶Sr up to 0.70642 ± 2 (refs. 24,25). The Unit 10 troctolite could have acquired its ⁸⁷Sr/⁸⁶Sr composition by mixing of ~7% Archaean (Lewisian Complex) quartzo-feldspathic gneiss with

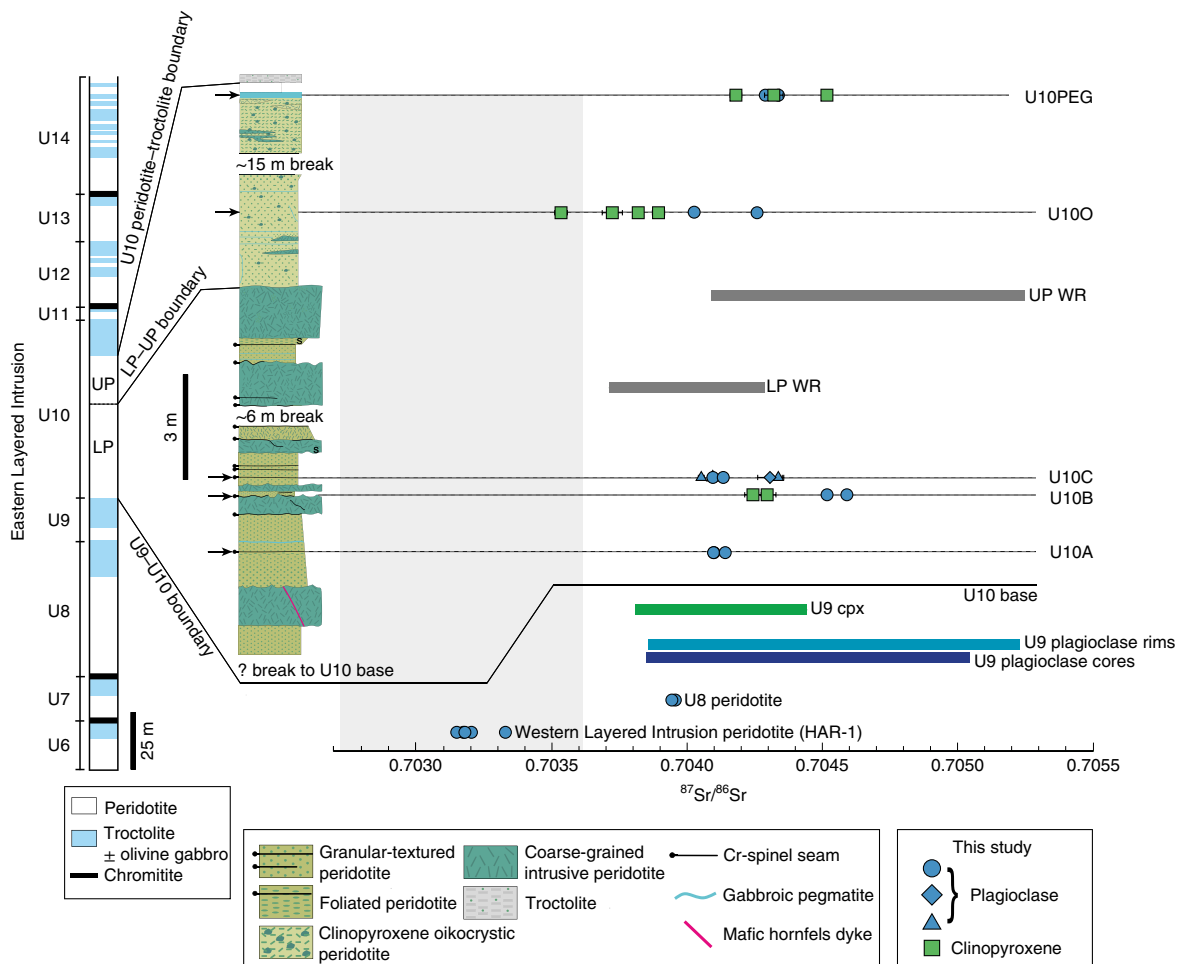


Fig. 2 | Comparison of new plagioclase and clinopyroxene $^{87}\text{Sr}/^{86}\text{Sr}$ data with a compilation of published data for the Rum intrusion. Included are the $^{87}\text{Sr}/^{86}\text{Sr}_{\text{initial}}$ range of three Rum picrites (grey field)²⁹, Unit 10 bulk rock (WR) data²⁴ and Unit 9 clinopyroxene and plagioclase data²³. Petrological context for sampled localities in the Unit 10 lower and upper peridotites (LP and UP, respectively) is shown in the schematic logs on the left. Uncertainties in the new $^{87}\text{Sr}/^{86}\text{Sr}$ data are 2σ and are typically smaller than symbol sizes. Where different symbols are shown at a given stratigraphic level, this denotes analysis of different crystals.

Rum picrite²⁴. Binary mixing calculations suggest that reaction of picrite ($^{87}\text{Sr}/^{86}\text{Sr}=0.702705$, 244 ppm Sr (ref. ²⁹)) and cumulate (for example, $^{87}\text{Sr}/^{86}\text{Sr}=0.70578$, 282 ppm Sr; Unit 10 troctolite²⁴) require the most-radiogenic compositions in our new dataset to have sourced >50% of their Sr from the cumulate. The reactive percolation process was thus capable of ‘recycling’ crustal $^{87}\text{Sr}/^{86}\text{Sr}$ signatures in the Rum system at the postcumulus stage. Mass balance considerations for Cr and the PGEs also require melt through-flow to have occurred. For example, Unit 10 Cr-spinel seams can contain ~100 ppb Pt²⁵, which is ~25 times the amount of Pt that could have been concentrated from a 1-mm-thick layer of picrite melt²⁰. The PGEs are mainly associated with base-metal sulfides, which we interpret as by-products of the melt-rock reaction process.

Fluid dynamics and timescales of cooling

It is possible to place further constraints on the nature of the percolation zones in which the Cr-spinel seams formed. A critical observation is that many Unit 10 Cr-spinel seams extend laterally along strike for several tens of metres without significant thickness changes. The primary controls on fluid flow through a dissolvable matrix can be described by the Damköhler number (Da), which relates the amount of reaction that occurs to the flow rate over a characteristic length scale^{30,31}:

$$\text{Da} = \frac{R_{\text{eff}}L}{\rho_{\text{fluid}}\phi_0\omega_0}$$

The equilibration length (L_{eq}) describes how far the melt may advect before equilibrating with the host rock:

$$L_{\text{eq}} = \frac{\rho_{\text{fluid}}\phi_0\omega_0}{R_{\text{eff}}}$$

where R_{eff} is an effective reaction rate constant (in $\text{kg m}^{-2}\text{s}^{-1}$), L is the characteristic length scale, ρ_{fluid} is the density of the invading melt and ω_0 is the melt flow rate at porosity ϕ_0 . Values of R_{eff} can be calculated using the dissolution experiments of Donaldson³², and ω_0 using Darcy’s law for melt flow through a porous matrix. Assuming a viscosity of 10 Pa s for the invading picrite, the formation of percolation zones extending 50–100 m along strike require a Da of ~ 10^4 and L_{eq} of 2–3 mm. These estimates imply very high degrees of reaction relative to melt flux. As well as underlining the requirement for through-flow of melt as discussed above, they highlight the importance of reactive picritic melts to the formation of Cr-spinel seams and associated PGE enrichment. It is plausible that zones of porous reactive melt percolation changed laterally to reaction within a hot tear, and back again, facilitating the formation of the seams over the

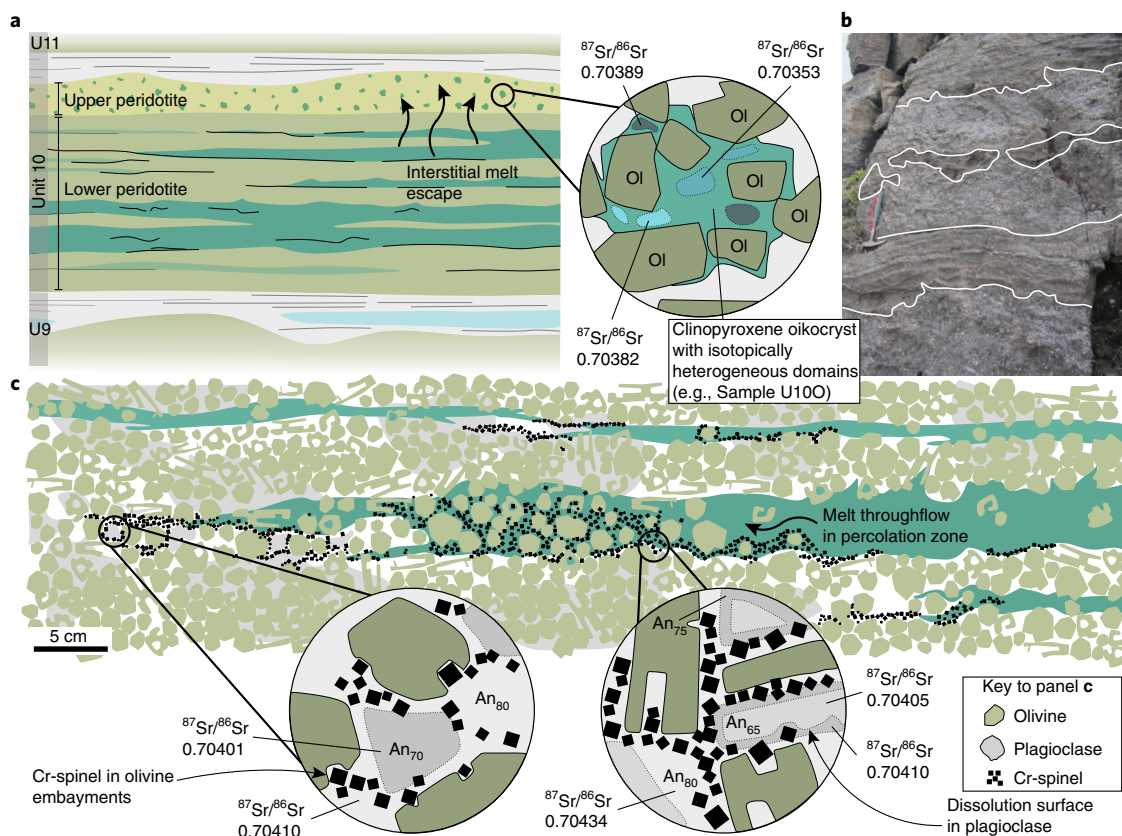


Fig. 3 | Schematic cartoon illustrating the reactive percolation model discussed in the text. a, The entire Unit 10 sequence. **b**, Representative field photograph showing typical distributions of intrusive peridotite (highlighted) in outcrop. **c**, Conceptual illustration (based on the field relationships) of the formation of strontium isotope heterogeneities ($^{87}\text{Sr}/^{86}\text{Sr}$ values are indicative only) during the formation of one percolation zone (scale is approximate). Note the leading fronts or basal/top contacts of percolation zones (dark green) locally develop chromitite *sensu stricto*, whereas chain-textured Cr-spinel seams signifying porous reactive flow form around olivine crystals. Reactive percolation zones may locally thin, thicken and bifurcate. The presence of >100 Cr-spinel seams throughout the Unit 10 lower peridotite implies that numerous percolation zones such as those illustrated in **c** must have existed. The observation that some Cr-spinel seams bifurcate means that the number of replenishments may be less than the number of Cr-spinel seams, and there is no requirement in our model for ‘stratigraphically’ higher Cr-spinel seams to postdate those that lie underneath them.

observed length scales (Fig. 3). Although it is likely that numerous percolation events are represented by the Unit 10 Cr-spinel seams, not all of them need have formed at different times. The observation that Cr-spinel seams may bifurcate implies that there are probably subsets of seams associated with single injections of picritic magma. Thus, the >100 Unit 10 seams represent a smaller number of intrusive replenishments. However, if branching networks of percolation zones existed, vertical separation of each zone by >10 cm of peridotite would have been required to allow disequilibrium transport, assuming no interchannel porosity.

Allowing for through-flow of reactive picrite, another question concerns the ultimate fate of this melt, as well as the interstitial melt present before reactive percolation. Hepworth et al.²⁵ reported the presence of vertically elongate clinopyroxene crystals in the lower peridotite resembling fluid escape structures. The single clinopyroxene oikocryst analysed from the upper peridotite has less radiogenic Sr than any of the plagioclase analysed in this study, despite the bulk rock upper peridotite compositions being significantly more radiogenic than the lower peridotite bulk rocks²⁴. This is consistent with the clinopyroxene oikocrysts of the upper peridotite pseudomorphing melts that escaped from the underlying cumulate pile following emplacement of the lower peridotite. The pegmatite body at the top of the upper peridotite probably formed from isotopically distinct melts that ponded and solidified beneath the overlying relatively impermeable cap represented by the Unit 10 troctolite.

The preservation of intracrystalline Sr heterogeneity has implications for the timescales of cooling of the Unit 10 peridotite. Using experimentally derived diffusion coefficients for Sr in plagioclase and diopside^{33,34}, it is possible to calculate diffusive equilibration times for Sr in these phases. Diffusion of Sr is faster in diopside (Fig. 4a), but the heterogeneities we observe in the oikocryst are on the order of millimetres apart (Fig. 1b). The Sr variations in plagioclase, on the order of 10–100 μm apart, point to the shortest timescales for cooling in the Rum intrusion. Following Reddy et al.³⁵ and subsequently Tepley and Davidson²³, diffusivity can be calculated as a function of cooling rate. In Fig. 4b, *a* is the length scale over which diffusion of Sr in anorthite can occur and is plotted against time for cooling rates of 1 $^{\circ}\text{C}$, 0.1 $^{\circ}\text{C}$ and 0.01 $^{\circ}\text{C}$ per year. Three possible starting temperatures are considered, 1,100 $^{\circ}\text{C}$, 1,150 $^{\circ}\text{C}$ and 1,200 $^{\circ}\text{C}$. Although the liquidus temperature of the incoming picrite was probably higher initially, assimilation of feldspathic cumulate probably reduced this to temperatures in the range of those used in the calculations. The calculations suggest that to achieve Sr heterogeneities over the length scales observed, cooling rates were probably in excess of 1 $^{\circ}\text{C}$ per year, and cooling to below closure temperatures must have occurred within tens to hundreds of years, orders of magnitude faster than suggested by Tepley and Davidson²³.

An important implication of these calculations as well as our observations more generally is that crystal mushes associated with mafic magmatic systems can form by repeated intrusive magma

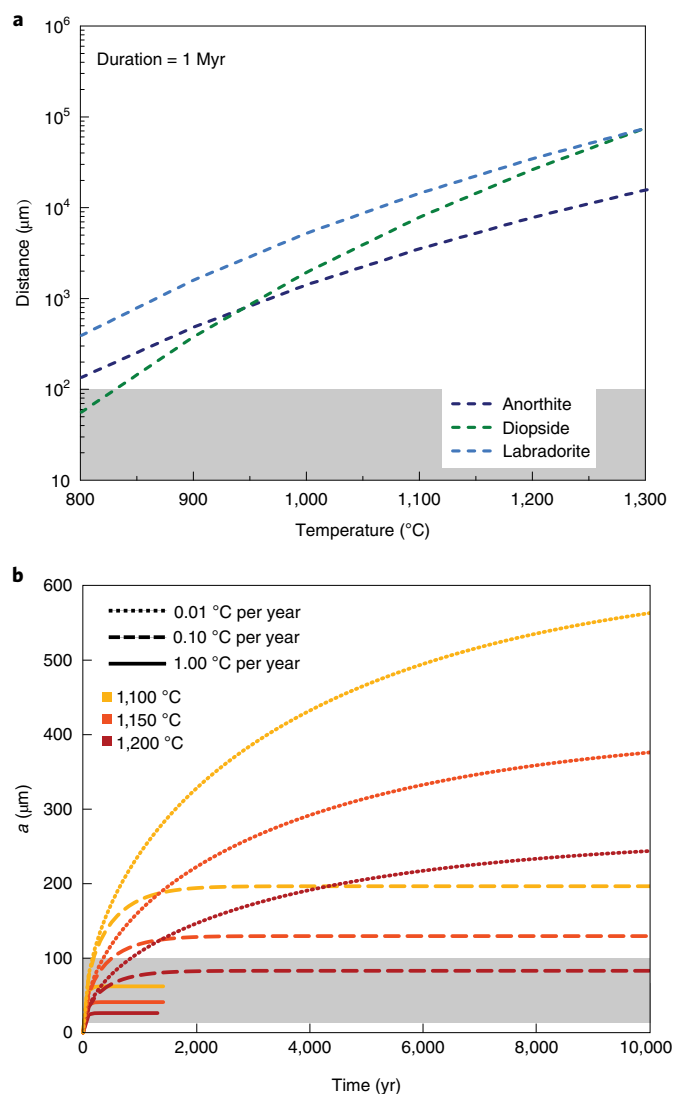


Fig. 4 | Diffusive equilibration calculations. **a**, Characteristic diffusion distance as a function of temperature for labradorite, anorthite and diopside. Over a duration of 1 Myr, estimated as the maximum time frame for cooling of the Rum intrusion^{17,23}, plagioclase Sr variation at 10–100 μm would not be preserved over the range of temperatures shown. **b**, Plot of calculated length scale of diffusion of Sr (a) versus time (yr) for anorthite. Sr isotope variations exist over length scales of 10–100 μm (grey shaded field along base of plot), so only curves contained completely within the field can be reconciled with our observations.

addition before complete solidification. Although our conclusions do not preclude other parts of the Rum intrusion forming more conventionally (for example, crystal settling, in situ crystallization at magma chamber margins), our findings are incompatible with the traditional view of layered intrusion formation by uninterrupted cooling and solidification of a magma chamber. With respect to precious-metal mineralization elsewhere on Rum, PGE-rich chromitites at unit boundaries previously attributed to reactions on the magma chamber floor^{20,22} represent an important target for future research in light of the data presented here.

There is some uncertainty associated with extrapolating the model presented here to precious-metal-bearing chromitites in larger, economically significant layered intrusions such as the Bushveld and Stillwater complexes. However, high-resolution (uranium–lead in zircon) age determinations from cumulates in both of

those intrusions attributed the presence of rocks with younger ages underlying those with older ages to periodic intrusion of magma into the crystal mush^{36–38}, associated with important PGE deposits in both cases. The latter studies have not gone unchallenged^{39,40}, but when combined with the evidence presented here for rapid crystallization of mafic crystal mushes during repeated self-intrusion of magma, it is clear the long-held paradigm that all layered intrusions form by solidification from the bottom up (and/or top down) requires re-evaluation. Our new data highlight the potential for partly solidified mafic crystal mush zones existing in ‘cold storage’ to be rejuvenated by new magma input, as has been increasingly recognized in recent years for silicic magmatic systems^{15,16,41}.

Online content

Any methods, additional references, Nature Research reporting summaries, source data, extended data, supplementary information, acknowledgements, peer review information; details of author contributions and competing interests; and statements of data and code availability are available at <https://doi.org/10.1038/s41561-020-0568-3>.

Received: 15 October 2019; Accepted: 9 March 2020;

Published online: 13 April 2020

References

- Cawthorn, R. G., Barnes, S. J., Ballhaus, C. & Malitch, K. N. in *Economic Geology: One Hundredth Anniversary Volume, 1905–2005* (eds Hedenquist, J. W. et al.) 215–249 (Society of Economic Geologists, 2005).
- Naldrett, A. J. *Magmatic Sulfide Deposits: Geology, Geochemistry and Exploration* (Springer Verlag, 2004).
- Naldrett, A. J. & Duke, J. M. Platinum metals in magmatic sulfide ores. *Science* **208**, 1417–1424 (1980).
- Eales, H. V. & Cawthorn, R. G. in *Layered Intrusions* (ed. Cawthorn, R. G.) 181–230 (Elsevier, 1996).
- Godel, B. in *Layered Intrusions* (eds Charlier, B. et al.) 379–432 (Springer Science, 2015).
- Mungall, J. E. & Naldrett, A. J. Ore deposits of the platinum-group elements. *Elements* **4**, 253–258 (2008).
- Latypov, R., Chistyakova, S., Page, A. & Hornsey, R. Field evidence for the in situ crystallization of the Merensky Reef. *J. Petrol.* **56**, 2341–2372 (2015).
- Naldrett, A. J., Gasparini, E. C., Barnes, S. J., Von Gruenewaldt, G. & Sharpe, M. R. The upper critical zone of the Bushveld Complex and the origin of Merensky-type ores. *Econ. Geol.* **81**, 1105–1117 (1986).
- Boudreau, A. E. & McCallum, I. S. Concentration of platinum-group elements by magmatic fluids in layered intrusions. *Econ. Geol.* **87**, 1830–1848 (1992).
- Boudreau, A. Fluid fluxing of cumulates: the J-M reef and associated rocks of the Stillwater complex, Montana. *J. Petrol.* **40**, 755–772 (1999).
- Namur, O. et al. in *Layered Intrusions* (eds Charlier, B. et al.) 75–152 (Springer Science, 2015).
- Holness, M. B., Humphreys, M. C. S., Sides, R., Helz, R. T. & Tegner, C. Toward an understanding of disequilibrium dihedral angles in mafic rocks. *J. Geophys. Res. Solid Earth* **117**, B06207 (2012).
- Cashman, K. V., Sparks, R. S. J. & Blundy, J. D. Vertically extensive and unstable magmatic systems: a unified view of igneous processes. *Science* **355**, eaag3055 (2017).
- Annen, C., Blundy, J. D. & Sparks, R. S. J. The genesis of intermediate and silicic magmas in deep crustal hot zones. *J. Petrol.* **47**, 505–539 (2006).
- Claiborne, L. L., Miller, C. F., Flanagan, D. M., Clyne, M. A. & Wooden, J. L. Zircon reveals protracted magma storage and recycling beneath Mount St. Helens. *Geology* **38**, 1011–1014 (2010).
- Cooper, K. M. & Kent, A. J. R. Rapid remobilization of magmatic crystals kept in cold storage. *Nature* **506**, 480–483 (2014).
- Emeleus, C. H., Cheadle, M. J., Hunter, R. H., Upton, B. G. J. & Wadsworth, W. J. in *Layered Igneous Rocks. Developments in Petrology* Vol. 15 (ed. Cawthorn, R. G.) 404–440 (Elsevier Science, 1996).
- Brown, G. M. The layered ultrabasic rocks of Rhum, Inner Hebrides. *Philos. Trans. R. Soc. Lond. B* **668**, 1–53 (1956).
- Bédard, J. H., Sparks, R. S. J., Renner, R., Cheadle, M. J. & Hallworth, M. A. Peridotite sills and metasomatic gabbros in the Eastern Layered Series of the Rhum Complex. *J. Geol. Soc. Lond.* **145**, 207–224 (1988).
- O’Driscoll, B., Day, J. M. D., Daly, J. S., Walker, R. J. & McDonough, W. F. Rhenium-osmium isotopes and platinum-group elements in the Rum Layered Suite, Scotland: implications for Cr-spinel seam formation and the composition of the Iceland mantle anomaly. *Earth Planet. Sci. Lett.* **286**, 41–51 (2009).

21. Hamilton, M. A., Pearson, D. G., Thompson, R. N., Kelley, S. P. & Emeleus, C. H. Rapid eruption of Skye lavas inferred from precise U–Pb and Ar–Ar dating of the Rum and Cuillin plutonic complexes. *Nature* **394**, 260–263 (1998).
22. O'Driscoll, B., Emeleus, C. H., Donaldson, C. H. & Daly, J. S. Cr-spinel seam petrogenesis in the Rum Layered Suite, NW Scotland: cumulate assimilation and in situ crystallization in a deforming crystal mush. *J. Petrol.* **51**, 1171–1201 (2010).
23. Tepley, F. J. III & Davidson, J. P. Mineral-scale Sr-isotope constraints on magma evolution and chamber dynamics in the Rum layered intrusion, Scotland. *Contrib. Mineral. Petrol.* **145**, 628–641 (2003).
24. Palacz, Z. A. & Tait, S. R. Isotopic and geochemical investigation of unit 10 from the Eastern Layered Series of the Rhum intrusion, Northwest Scotland. *Geol. Mag.* **122**, 485–490 (1985).
25. Hepworth, L. N., O'Driscoll, B., Gertisser, R., Daly, J. S. & Emeleus, C. H. Incremental construction of the Unit 10 peridotite, Rum Eastern Layered Intrusion, NW Scotland. *J. Petrol.* **58**, 137–166 (2017).
26. Holness, M. B., Hallworth, M. A., Woods, A. & Sides, R. E. Infiltration metasomatism of cumulates by intrusive magma replenishment: the Wavy Horizon, Isle of Rum, Scotland. *J. Petrol.* **48**, 563–587 (2007).
27. Leuthold, J., Blundy, J. D., Holness, M. B. & Sides, R. Successive episodes of reactive liquid flow through a layered intrusion (Unit 9, Rum Eastern Layered Intrusion, Scotland). *Contrib. Mineral. Petrol.* **167**, 1021–1038 (2014).
28. Morse, S. A. *Basalts and Phase Diagrams* (Springer, 1980).
29. Upton, B. G. J. et al. Picritic magmas and the Rum ultramafic complex, Scotland. *Geol. Mag.* **139**, 437–452 (2002).
30. Pec, M., Holtzman, B. K., Zimmerman, M. & Kohlstedt, D. L. Reaction infiltration instabilities in experiments on partially molten mantle rocks. *Geology* **43**, 575–578 (2015).
31. Spiegelman, M., Kelemen, P. B. & Aharonov, E. Causes and consequences of flow organization during melt transport: the reaction infiltration instability in compactible media. *J. Geophys. Res. Solid Earth* **106**, 2061–2077 (2001).
32. Donaldson, C. H. The rates of dissolution of olivine, plagioclase and quartz in a basaltic melt. *Mineral. Mag.* **49**, 683–693 (1985).
33. Gilletti, B. J. & Casserly, J. E. D. Strontium diffusion kinetics in plagioclase feldspars. *Geochim. Cosmochim. Acta* **58**, 3785–3793 (1994).
34. Sneeringer, M., Hart, S. R. & Shimizu, N. Strontium and samarium diffusion in diopside. *Geochim. Cosmochim. Acta* **48**, 1589–1608 (1984).
35. Reddy, S. M., Kelley, S. P. & Wheeler, J. A. $^{40}\text{Ar}/^{39}\text{Ar}$ laser probe study of micas from the Seisa zone, Italian Alps: implications for metamorphic and deformation histories. *J. Metamorph. Geol.* **14**, 493–508 (1996).
36. Mungall, J. E., Kamo, S. L. & McQuade, S. U–Pb geochronology documents out-of-sequence emplacement of ultramafic layers in the Bushveld Igneous Complex of South Africa. *Nat. Commun.* **7**, 13385 (2016).
37. Robb, S. J. & Mungall, J. E. Testing emplacement models for the Rustenburg Layered Suite of the Bushveld Complex with numerical heat flow models and plagioclase geospeedometry. *Earth Planet. Sci. Lett.* **534**, 116084 (2020).
38. Wall, C. J. et al. The Stillwater Complex: integrating zircon geochronological and geochemical constraints of the age, emplacement history and crystallization of a large, open-system layered intrusion. *J. Petrol.* **59**, 153–190 (2018).
39. Latypov, R., Chistyakova, S. & Kramers, J. Arguments against syn-magmatic sills in the Bushveld Complex. *S. Afr. J. Geol.* **120**, 565–574 (2017).
40. Latypov, R. M. Comment on “The Stillwater Complex: integrating zircon geochronological and geochemical constraints on the age, emplacement history and crystallization of a large, open-system layered intrusion” by Wall et al. (*J. Petrology*, 59, 153–190, 2018). *J. Petrol.* **59**, 153–190 (2019).
41. Miller, C. F. et al. Growth of plutons by incremental emplacement of sheets in a crystal-rich host: evidence from Miocene intrusions of the Colorado River region, Nevada, USA. *Tectonophysics* **500**, 65–77 (2011).

Publisher's note Springer Nature remains neutral with regard to jurisdictional claims in published maps and institutional affiliations.

© The Author(s), under exclusive licence to Springer Nature Limited 2020

Methods

Mineral chemistry. Plagioclase mineral chemical data were obtained using a JEOL JXA-8900RL electron microprobe at the Department of Geochemistry, Geowissenschaftliches Zentrum der Universität Göttingen in 2015. The plagioclase compositions were obtained using an acceleration voltage of 20 kV with a beam current of ~80 nA and a typical beam diameter of 20–25 µm. Plagioclase count times on peak and background for silicon (Si), calcium (Ca), Al, sodium (Na) and potassium (K) were 15 s and 5 s, respectively, for Fe were 30 s and 15 s, for Sr and Ba were 360 s and 180 s, respectively, and for titanium (Ti) were 300 s and 150 s, respectively. Clinopyroxene compositions were obtained with an acceleration voltage of 15 kV, a beam current of 15 nA and a typical beam diameter of 15 µm. Clinopyroxene count times on peak and background for Si, Na, K, Ti, Fe, Al, magnesium (Mg), Ca and manganese (Mn) were 15 s and 5 s, respectively, and 30 s and 15 s for Cr and nickel (Ni), respectively. Element maps of Na and Ca concentrations were obtained of plagioclase zoning, and for Cr, Mg, Ti and Al zoning in a clinopyroxene oikocryst from the Unit 10 upper peridotite (see also Hepworth et al.²³). Element maps were obtained using an acceleration voltage of 20 kV, with a beam current of ~60 nA, a beam diameter of 2 µm and a dwell time of 50 ms.

Strontium isotope measurements. Back-scattered electron images of zoned intercumulus plagioclase were obtained during mineral chemical analysis of peridotite thick sections (>200 µm) using a JEOL JXA-8900RL electron microprobe at the Department of Geochemistry, Geowissenschaftliches Zentrum der Universität Göttingen in 2015. Micro-milling targets were then carefully selected on the basis of criteria such as drill-bit diameter (75–200 µm), least potential mixing and maximum possible sample excisable (with plagioclase ~400 ppm Sr). Once samples were selected, they were drilled using a New Wave Micromill at the National Centre for Isotope Geochemistry at University College Dublin following the methods of Davidson et al.⁴² and Charlier et al.⁴³. Mixing between zones was avoided by careful sample selection, and although some blending during drilling may have occurred, it was considered to be minimal on the basis of the internal reproducibility between similar samples. Zones were drilled through a bead of 20 µl of millipure water to produce a slurry, which was then collected into a clean beaker (which itself was weighed before use), before a further 10 µl of millipure water was placed onto the sample site to collect any remaining sample. To digest the plagioclase residue, 0.8 ml of HF and 0.2 ml of HNO₃ were added to the beaker containing the sample, which was then sealed and left on a hot plate overnight (>12 h). After digestion, the solutions were dried under clean air on a hot plate. After cooling, samples were further digested in closed beakers in 0.3 ml aliquots of first concentrated HNO₃ and later in 0.3 ml of ~4 M HNO₃ (to break down any fluorides possibly present), drying between successive digestions. Subsequently, 0.3 ml of 1 M HNO₃ was added to the sample beakers, which were left to cool. Ion chromatography was carried out in disposable columns fashioned from pre-cleaned disposable pipette tips using ~100 mg of Eichrom SrSPEC (100–150 µm) resin supported on pre-cleaned Teflon frits. Columns were washed with 0.05 M HNO₃–8 M HNO₃–0.05 M HNO₃–1 M HNO₃ immediately prior to use. Following sample addition, 1 ml 1 M HNO₃ was eluted and discarded, followed by 8 M HNO₃ (to remove Ba). The Sr fraction was stripped from the columns using 2 ml 0.05 M HNO₃. Then 0.05 ml (50 µl) was pipetted from the collected Sr solutions and made up to ~3% HNO₃ and centrifuged at 5,000 rpm, and Sr concentrations were determined using a ThermoScientific Neptune Multiple Collector inductively coupled plasma mass spectrometer, calibrated against standard solutions. This served to estimate the amount of Sr available for thermal ionization mass spectrometry and provided an estimate of the ⁸⁷Sr/⁸⁶Sr ratio. The ⁸⁷Sr/⁸⁶Sr ratios were determined by thermal ionization mass spectrometry on a ThermoScientific Triton instrument using Sr loads, typically ranging in mass from ~20–100 ng (average = ~40 ng) for plagioclase and ~10 ng for clinopyroxene. The Sr fractions (aliquoted if necessary to optimize the loaded mass) were taken up in 1 µl of 0.05 M HNO₃ and loaded onto Re filaments with 1 µl of tantalum (Ta) activator (TaCl₅). An age correction of ~60 Myr (ref. ²¹) is not necessary given analytical uncertainty and Rb concentrations <1 ppm in plagioclase²³. We assume that this assumption applies to clinopyroxene too, on the basis of concentrations of 100–200 ppb Rb reported by Leuthold et al.²⁷ for clinopyroxenes in the adjacent Unit 9 rocks. The Sr concentrations in the blanks were <0.02 ng, and repeat measurements of reference material NBS SRM 987

using sample loads of 20 ng and 50 ng (see Supplementary Table 4 in Supplementary Data 1) yielded a mean ⁸⁷Sr/⁸⁶Sr value of 0.710277 ± 31 (2σ, n = 13). This value is indistinguishable from the certified value (0.71034 ± 26) (ref. ⁴⁴) and from more-precise values, for example, 0.710249 ± 18 to 0.710269 ± 23, reported recently by Schannor et al.⁴⁵. The full dataset, including analytical uncertainties and standard analyses, can be found in Supplementary Table 4 in Supplementary Data 1.

Data availability

The data generated during this study are all accessible in the main article and accompanying supplementary data files, and have also been deposited with the National Geoscience Data Centre of the British Geological Survey (<https://dx.doi.org/10.5285/093ddaf1-789a-4b8f-aaca-af4d2f070134>). Source data are provided with this paper.

References

- Davidson, J. P., Tepley, F. J. III & Knesel, K. M. Isotopic fingerprinting may provide insights into evolution of magmatic systems. *EOS Trans.* **79**, 185, 189, 193 (1998).
- Charlier, B. L. A. et al. Methods for the microsampling and analysis of strontium and rubidium isotopes at single crystal scale for petrological and geochronological applications. *Chem. Geol.* **232**, 114–133 (2006).
- Certificate of Analysis: Standard Reference Material 987* (NIST, 2007).
- Schannor, M. et al. Small-scale Sr and O isotope variations through the UG2 in the eastern Bushveld Complex: the role of crustal fluids. *Chem. Geol.* **485**, 100–112 (2018).

Acknowledgements

L.N.H. acknowledges funding from a Natural Environmental Research Council (NERC) Studentship (grant no. 1361482) and Keele University. We thank Scottish National Heritage (SNH) for sampling permission on Rum during 2014 and 2015. We thank P. Greatbatch and D. Wilde (Keele University) for thin-section preparation and A. Kronz and G. Breedveld for assistance with EMPA analysis at the University of Göttingen. We also thank H. Horsch for her assistance generating the QEMSCAN images and M. Murphy (UCD) for technical assistance. Strontium isotopic analyses were carried out at the National Centre for Isotope Geochemistry (NCIG), Dublin, which is a joint venture of University College Dublin, Trinity College Dublin, University College Cork and National University of Ireland Galway, funded mainly by Science Foundation Ireland, including grant no. 04/BR/ES0007/EC07 awarded to J.S.D. J.S.D. was also supported in part by Science Foundation Ireland grant no. 13/RC/2092, which is co-funded under the European Regional Development Fund. We thank J. Day for helpful comments on an earlier version of the manuscript.

Author contributions

B.O'D. conceived the study. B.O'D., L.N.H. and J.S.D. designed the programme of work. L.N.H. carried out fieldwork and EMPA analyses. L.N.H. and J.S.D. carried out the chemistry and mass spectrometry for strontium isotope analysis. B.O'D. and C.G.J. did the Sr diffusion-related calculations. All authors contributed to interpreting the results. B.O'D. wrote the manuscript. B.O'D., J.S.D., L.N.H., R.G. and C.G.J. contributed to editing the final version.

Competing interests

The authors declare no competing interests.

Additional information

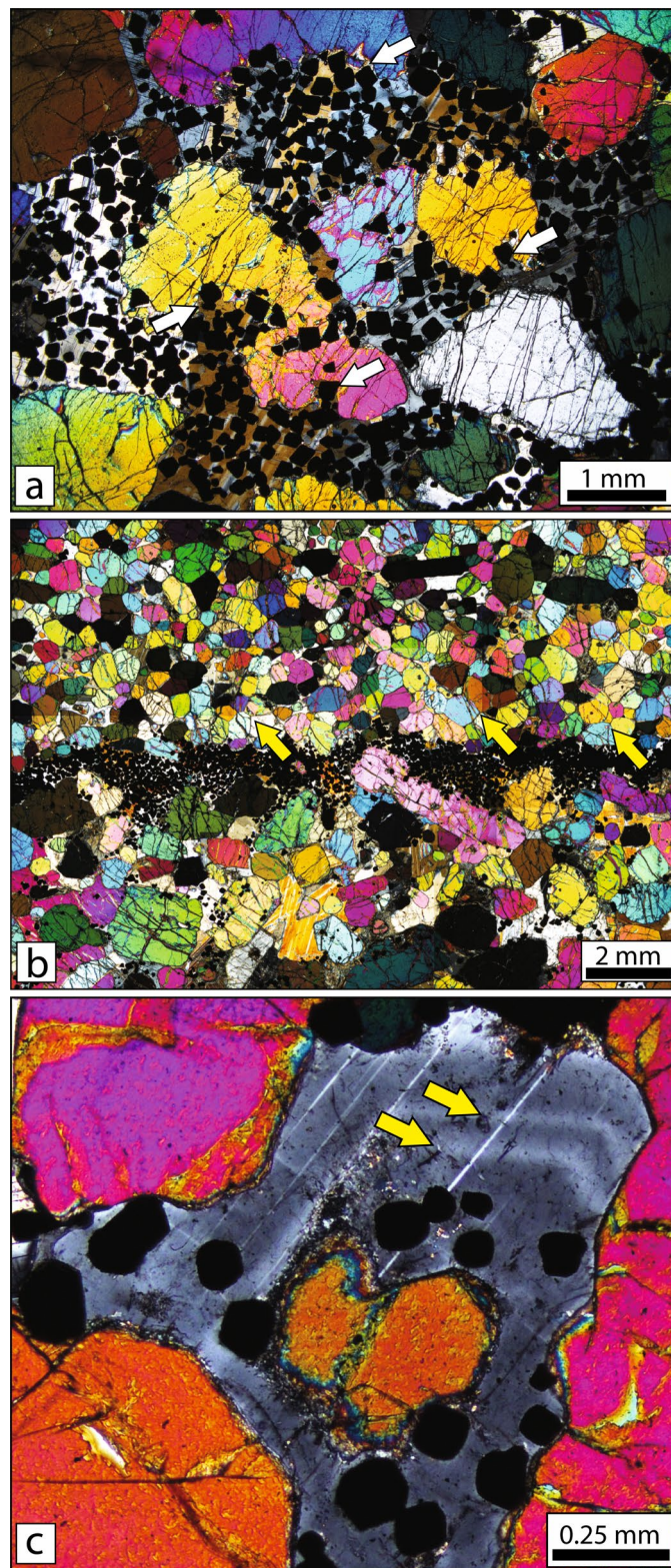
Extended data is available for this paper at <https://doi.org/10.1038/s41561-020-0568-3>.

Supplementary information is available for this paper at <https://doi.org/10.1038/s41561-020-0568-3>.

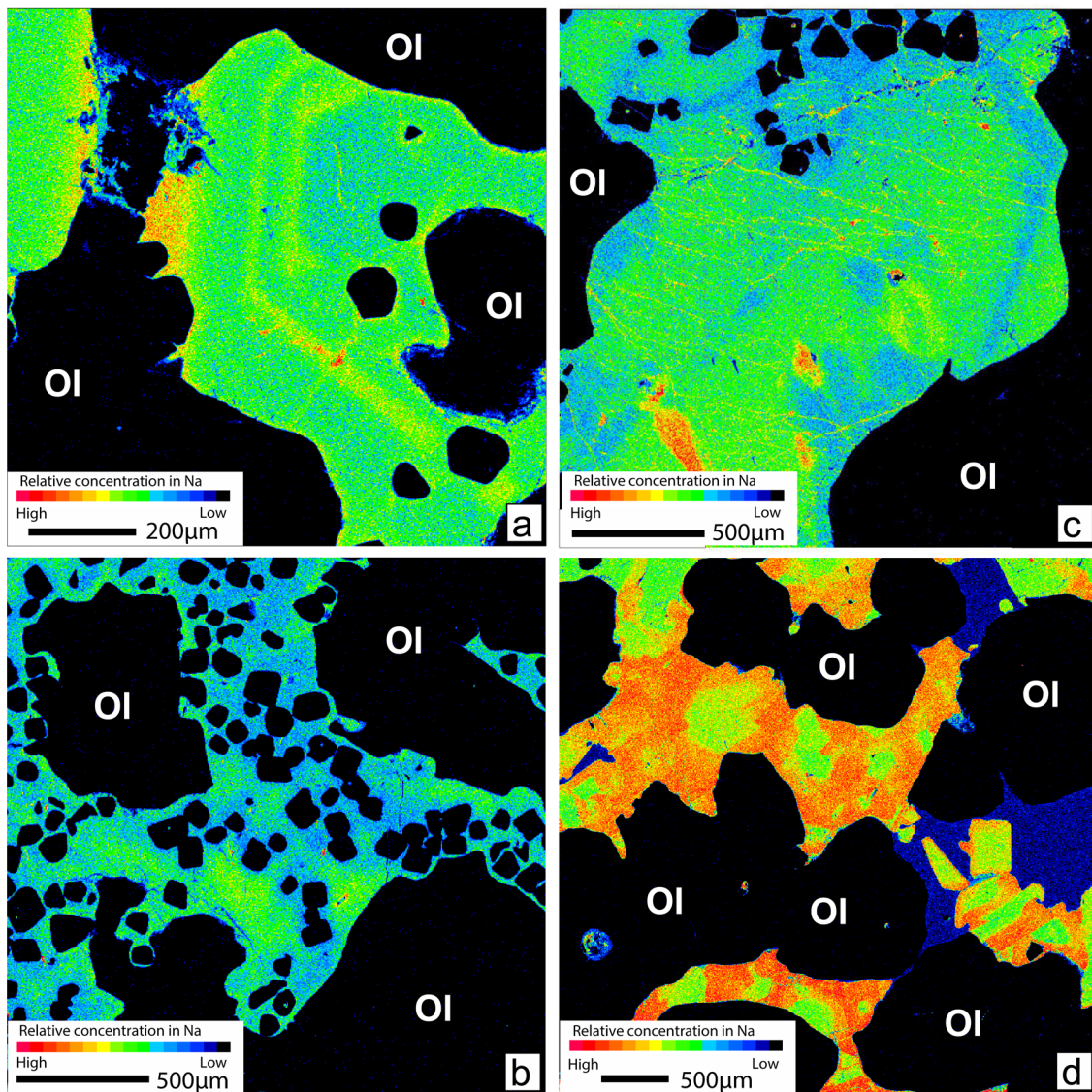
Correspondence and requests for materials should be addressed to B.O'D.

Peer review information Primary Handling Editor: Rebecca Neely.

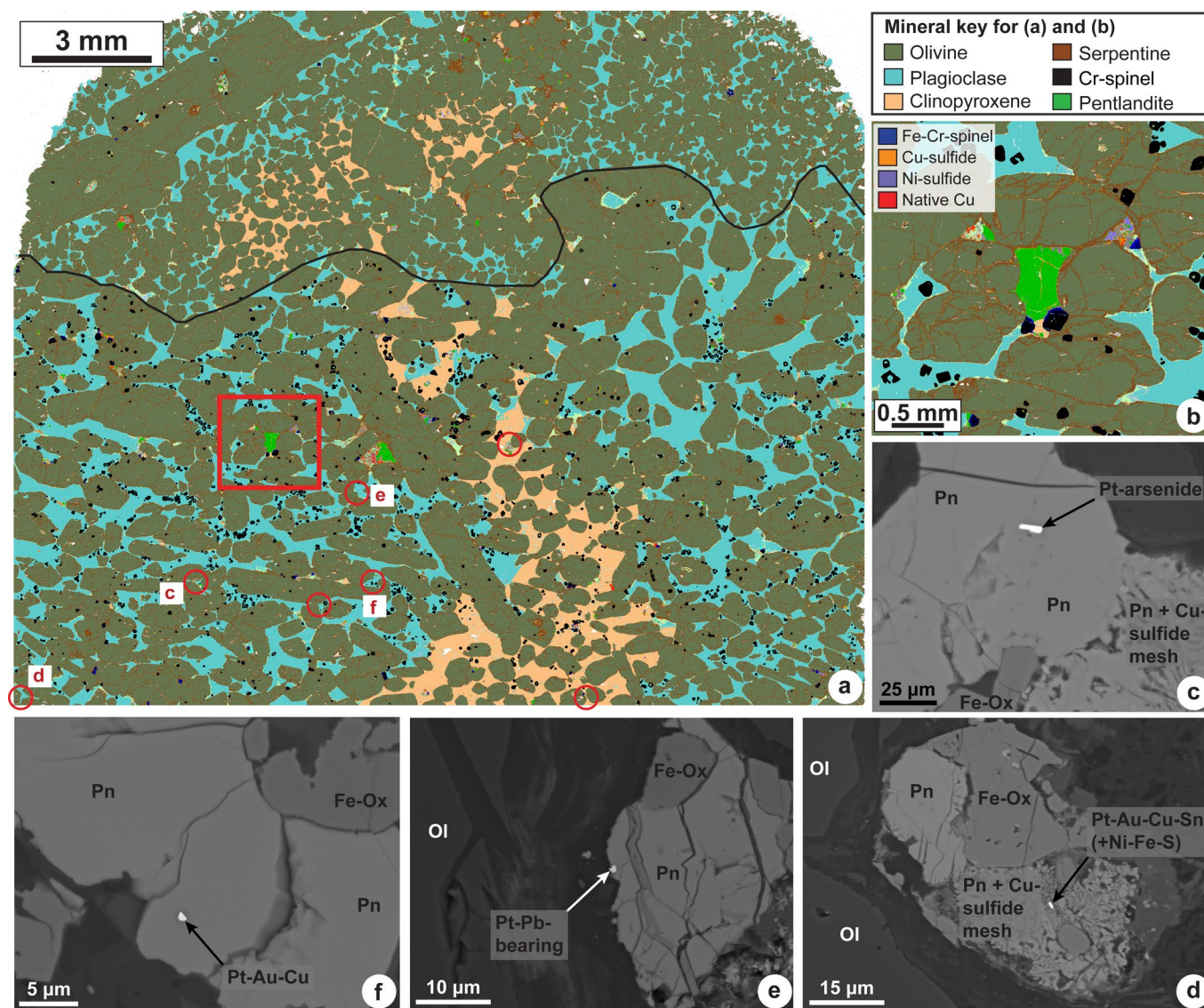
Reprints and permissions information is available at www.nature.com/reprints.



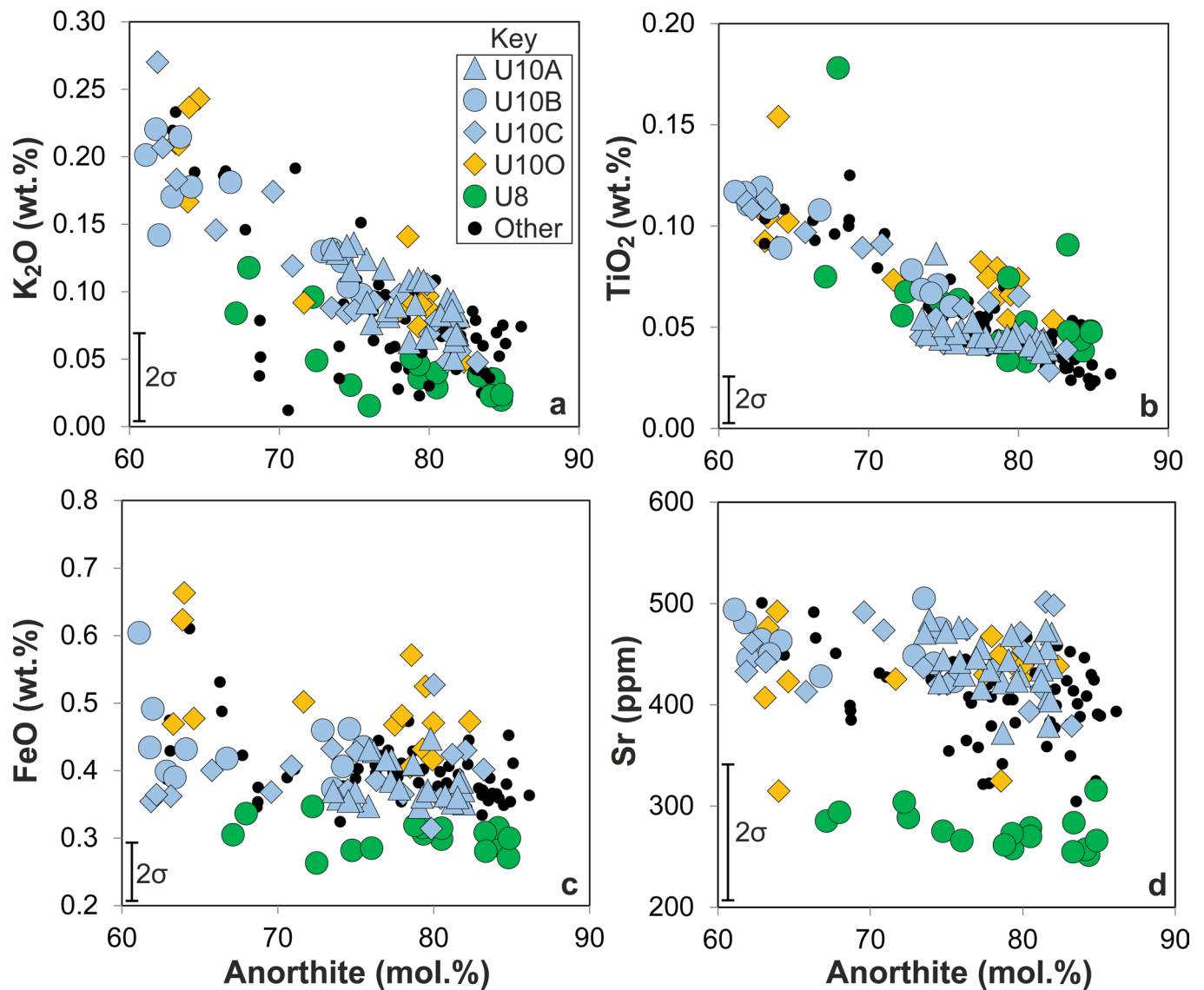
Extended Data Fig. 1 | Thin section photomicrographs of Unit 10 Cr-spinel seams. Transmitted light (crossed polars) photomicrographs of microstructures associated with the lower peridotite Cr-spinel seams. **a**, Chain-textured arrangement of Cr-spinel around olivine primocrysts (and embedded in interstitial plagioclase) in a typical ~1-cm-thick seam. The white arrows point to embayments in olivine crystals that are occupied by Cr-spinel crystals. **b**, Example of a much less diffuse Cr-spinel seam than in (a) (black; this one may be chromitite proper). Note the olivine primocryst grainsize change across the seam. The yellow arrows point to the triple junctions between olivine crystals in the finer-grained peridotite, which suggest an approach to solid-state textural equilibrium. **c**, Oscillatory zoned interstitial plagioclase in a Cr-spinel seam. The brightly coloured crystals on all sides are olivine.



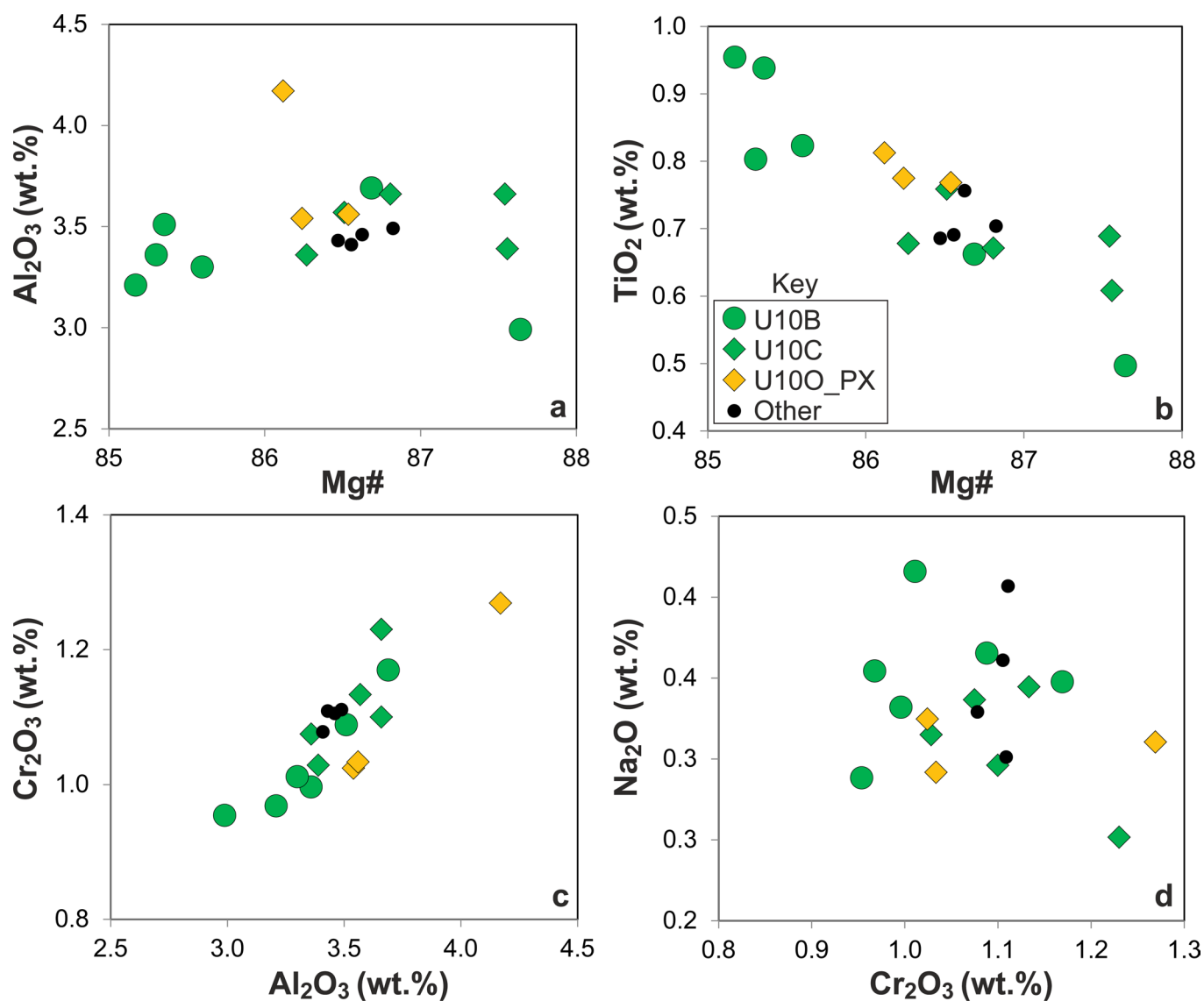
Extended Data Fig. 2 | Element maps of plagioclase in the Unit 10 lower peridotite. Element maps (Na) showing typical textures of intercumulus plagioclase in Cr-spinel seams from the Unit 10 lower peridotite. **a**, Oscillatory zoning of intercumulus plagioclase between olivine primocrysts. The smaller unlabelled black crystals are Cr-spinel. **b**, Chain-textured arrangement of Cr-spinel (small black-coloured) crystals around olivine crystals (labelled ol) in a Unit 10 Cr-spinel seam. Note the variation in intercumulus plagioclase composition and the tendency for Cr-spinel to occur in more anorthitic plagioclase. **c**, Compositional variation in intercumulus plagioclase from adjacent to a Unit 8 Cr-spinel seam. As for **(b)** above, note the occurrence of Cr-spinel in the more anorthitic plagioclase, supporting the argument that Cr-spinel crystallized by a peritectic reaction between picrite and relatively sodic plagioclase. **d**, Complex compositional variation in intercumulus plagioclase (orange-green). The blue-coloured crystal is clinopyroxene.



Extended Data Fig. 3 | QEMSCAN and back-scattered electron images of platinum-group mineral phases in a Unit 10 Cr-spinel seam. **a**, QEMSCAN image of diffuse platinum-group mineral bearing Cr-spinel seam illustrating the general distribution and style of PGE mineralization in the Unit 10 lower peridotite. The solid black line illustrates the top boundary of the seam. The lower boundary is more diffuse and is mainly out of the image frame. **b**, Close up image of the area outlined in the red box in **(a)**, illustrating the occurrence of sulfides at olivine three grain junctions. **c-f**, Back-scattered electron micrograph images of platinum-group minerals from the seam in **(a)**, associated with base-metal sulfides. The labelled red circles in **(a)** correspond to the locations in the sample of the images in c-f. Abbreviations as follows: Pn – pentlandite; Fe-ox – magnetite or ferrian Cr-spinel; ol – olivine.



Extended Data Fig. 4 | Unit 10 plagioclase mineral chemical data plots. Plagioclase compositional variations as measured by electron microprobe. **a–d**, are K₂O (wt.%), TiO₂ (wt.%), FeO (wt.%) and Sr (ppm) versus An content, respectively. The black-filled symbols represent analyses from Cr-spinel seams in the Unit 10 lower peridotites not studied further (i.e., for ⁸⁷Sr/⁸⁶Sr) here. Note the strong anti-correlation of plagioclase TiO₂ with anorthite content, linking the crystallization of Cr-spinel with that of relatively anorthitic plagioclase; with the onset of crystallization of Cr-spinel, Ti preferentially partitioned into it. Vertical bars show 2σ uncertainties.



Extended Data Fig. 5 | Unit 10 clinopyroxene mineral chemical data plots. Clinopyroxene compositional variations as measured by electron microprobe. **a**, Al₂O₃ (wt.%) versus Mg# [Mg# = Mg/(Mg+Fe²⁺+Mn)*100]; **b**, TiO₂ (wt.%) versus Mg#; **c**, Cr₂O₃ (wt.%) versus Al₂O₃ (wt.%); **d**, Na₂O (wt.%) versus Cr₂O₃ (wt.%). The black-filled symbols represent analyses from Cr-spinel seams in the Unit 10 lower peridotites not studied further (i.e., for ⁸⁷Sr/⁸⁶Sr).